

# Pressure Variations in Rocket Nozzles. Part 2: Analytical Predictions During Blowdown

Brian A. Maicke<sup>\*</sup> and Joseph Majdalani<sup>†</sup>  
*University of Tennessee Space Institute, Tullahoma, TN 37388*

and

Robert L. Geisler<sup>‡</sup>  
*Geisler Enterprises, Tehachapi CA 93561*

We consider the one-dimensional equations that delineate the operating modes of a converging-diverging nozzle over a range of chamber pressures. The main purpose of this study is to characterize the flow regimes experienced in the nozzle during the blowdown process at mission's end. Blowdown transients can lead to sideloads in the nozzle due to flow asymmetries including normal and oblique shock transitions, shock movement and excursions, flow separation, and the formation of recirculatory zones. By characterizing the nozzle flowfield with one-dimensional equations, we can achieve a direct analytical representation of the key pressure ratios that dictate the ensuing flow regime: supersonic with external shocks, supersonic with optimal expansion, supersonic with internal shocks, or subsonic throughout. These dividing pressure ratios are obtained using asymptotic methods that enable us to estimate the duration of the sideload flow regime by comparing the blowdown pressure profile to the delimiting pressure values projected by their corresponding asymptotic solutions. In fact, Part 1 of this investigation details the analytical methodology leading to closed-form representations of the pressure to an arbitrary level of precision (see Maicke, B. A., and Majdalani, J., "Pressure Variations in Rocket Nozzles. Part 1: Direct Asymptotic Predictions," AIAA Paper 2010-7072, July 2010). In this study, these solutions are inverted to the extent of predicting the nozzle flow conditions associated with an evolving chamber pressure, rather than a varying back pressure. The flow attributes of the various regimes and their corresponding shock transitions are subsequently explained in view of the pressure descent that accompanies chamber blowdown. We retire with a discussion of experimental observations involving slag accumulation and its effects on spin generation during tail off in the upper stage of a sounding rocket.

## Nomenclature

$A$	=	local cross sectional area
$A_t$	=	nozzle throat area
$c_1, c_2$	=	coefficients given by Eq. (18)
$p$	=	normalized pressure, $\bar{p}_c / \bar{p}_e$
$p_{opt}$	=	normalized exit pressure at optimal expansion, $\bar{p}_{opt} / \bar{p}_e$
$p_{sub}$	=	normalized exit pressure at initial choking, $\bar{p}_{sub} / \bar{p}_e$
$p_{sup}$	=	normalized exit pressure with shock in the exit plane, $\bar{p}_{sup} / \bar{p}_e$
$\alpha$	=	first exponent on the isentropic pressure equation, $-2/\gamma$
$\beta$	=	second exponent on the isentropic pressure equation, $-1-1/\gamma$

<sup>\*</sup>Graduate Research Assistant, Mechanical, Aerospace and Biomedical Engineering Department. Member AIAA.

<sup>†</sup>H. H. Arnold Chair of Excellence in Advanced Propulsion, Mechanical, Aerospace and Biomedical Engineering Department. Senior Member AIAA. Fellow ASME.

<sup>‡</sup>Senior Rocket Scientist, Associate Fellow AIAA.

- $\varepsilon$  = perturbation parameter,  $(A_t / A_e)^2$
- $\gamma$  = ratio of specific heats
- $\xi$  = constant related to  $\gamma$  via Eq. (4)

*Subscripts and Symbols*

- 0,1 = leading and first order
- c = condition in the chamber
- e = condition in the exit plane
- n = asymptotic level
- t = condition at the nozzle throat
- = condition before a normal shock (minus)
- + = condition after a normal shock (plus)
- = overbars denote dimensional quantities

**I. Introduction**

**N**OZZLE transients have long been a source of frustration for aerospace engineers. Though often short in duration, transient effects can lead to unpredictable vibrational loads on both the nozzle and vehicle structure. In addition to vibrations, persistent torques and sideloads are repeatedly shown to affect the mission profile. Sideloads have been observed in a number of different hardware configurations including the J2-S,<sup>1</sup> Vulcain,<sup>2</sup> LE-7A,<sup>3,4</sup> and the Space Shuttle Main Engine.<sup>5</sup> In some cases, the sideloads are severe enough to cause damage to both the structure and nozzles of these engines.

In order to understand the physical phenomena present during the blowdown process, it is first critical to understand how the nozzle behaves as variations in the pressure ratio are introduced. For a fully-flowing nozzle at the end of its mission, the nozzle often begins with under-expanded operation, denoted as region ① in Fig. 1. The higher exit plane pressure results in continued expansion as the flow exits the nozzle at supersonic speeds. When the motor finishes its burn, the chamber pressure decreases and the nozzle passes through the first delimiting pressure value at ②, thereby denoting a fully supersonic nozzle with no aftershock effects anywhere. This condition is considered to be the ideal/optimal operating case for the nozzle, although it rarely occurs near the end of rocket flight because of mission profile constraints. Instead, this ideal case is passed through at some point in the middle of the mission to prevent the early stages of the burn from experiencing severe overexpansion. After crossing this boundary, the flow enters the slightly over-expanded regime as illustrated in region ③. At this stage, oblique shocks form at the edges of the nozzle such that the lower exit pressure can increase to match

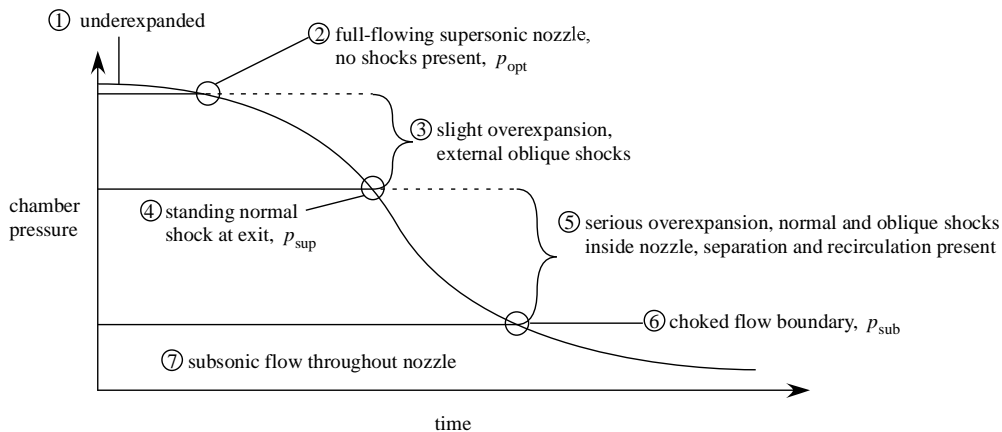


**Figure 1. Pressure trace of a rocket motor during blowdown.**

ambient conditions. These shocks remain external to the nozzle and, as such, have a limited effect on vehicle performance. As blowdown progresses, the chamber pressure continues to falter and the flowfield passes through a non-isentropic boundary point, a standing normal shock in the exit plane, labeled ④ in Figs. 1 and 2. Further decreases in the chamber pressure are characterized in region ⑤ where irreversible effects move into the nozzle and both normal and oblique shocks start to occur depending on nozzle shape and configuration. In addition to these shocks, flow separation and regions of recirculation can occur. As these processes unfold asymmetrically, the probability of a resulting net sideload increases. Then as the pressure decreases further, the flow passes through the choking boundary (labeled ⑥ in Figs. 1 and 2). It finally enters the region of fully subsonic flow. In this regime, the flow may no longer be predominantly axial given the absence of supersonic gas expansion in the streamwise direction. As a result, the orders of the velocity components become equalized to the extent that tangential velocities and forces may no longer be small relative to their counterparts in the axial direction. This is especially true during the evacuation phase of the flow that is often accompanied by the formation of bathtub vortices and throat reduction due to vortex blockage. Furthermore, as the fluid is cooled during the blowdown process, slag particles can solidify and present an increasingly important factor in drag generation.

It is possible to use one-dimensional nozzle theory to predict these transition points with varying degrees of accuracy. While this type of model cannot account for multi-dimensional effects, the predominantly axial flow through a supersonic nozzle can often be approximated through the use of quasi-one-dimensional expressions, namely Stodola's isentropic-area ratio equation. In this study, the Stodola area ratio expression will be combined with the equations for isentropic pressure behavior to determine an expression relating the pressure and area ratios. Additionally, the equation for the pressure jump across a normal shock will be used to predict the condition for which a normal shock will stand in the exit plane of a supersonic nozzle. These expressions will be systematically inverted, using asymptotic methods, to provide engineering approximations that can predict the transition points without resorting to numerical modeling or tabulation.

## II. Formulation

While the generation of sideloads cannot be handled one-dimensionally, the present model provides a fundamental starting point to separate these more complicated flow regions while retaining analytical closure. The boundaries labeled ② and ⑥ in Fig. 1 are generated using the isentropic pressure relation, reformulated in terms of the area ratio rather than the Mach number. It is given by

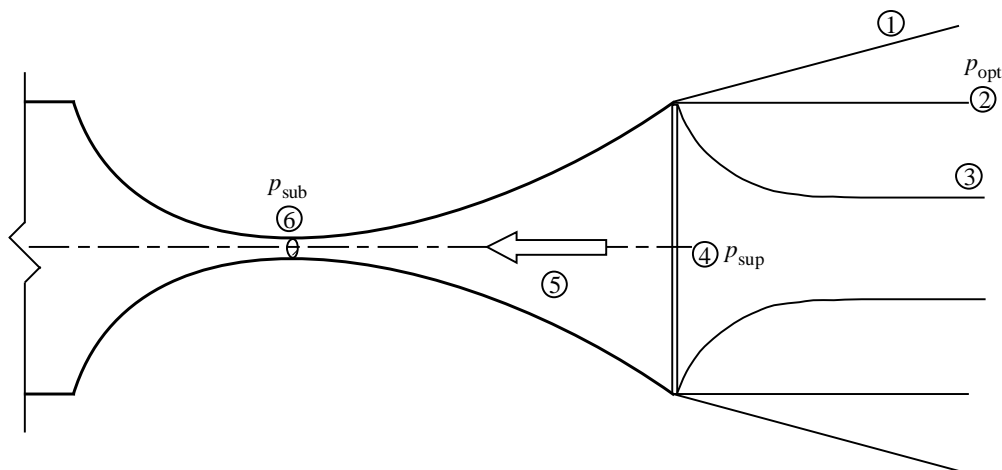


Figure 2. Various flow configurations with clearly labeled regions and threshold states during pressure blowdown.

$$p^{2/\gamma} (1 - p^{1-1/\gamma}) = \varepsilon \left( \frac{\gamma-1}{\gamma+1} \right) \left( \frac{2}{\gamma+1} \right)^{\frac{2}{\gamma-1}} \quad (1)$$

Here  $\varepsilon$  is the inverse of the expansion ratio squared,  $p$  is the pressure ratio  $\bar{p}_e / \bar{p}_c$ , and  $\gamma$  is the ratio of specific heats. There are two roots that emerge in an isentropic expansion. The first denotes the subsonic pressure ratio ⑥ at which the throat is first choked. The second refers to the supersonic root ② leading to optimal design conditions, with shock-free supersonic flow throughout. In Part 1, Eq. (1) is solved for  $\bar{p}_e / \bar{p}_c$ . This ratio is selected owing to a fast convergence rate, which can result in fewer terms for an acceptable solution. In the present study, the chamber pressure is the primary variable of interest and so, to facilitate comparisons to existing experimental and numerical work, it is useful to have the chamber pressure in the numerator of any ratio. This leads to two possible approaches: (a) solving for the faster converging ratio as in Part 1, and then inverting the final solution so that the chamber pressure appears in the numerator, or (b) inverting the ratio upfront and then solving the modified governing equation. Results from both methods will be compared in the following sections.

Before addressing the alternate formulations, it may be useful to recall that no isentropic solutions exist between the  $p_{\text{opt}}$  and  $p_{\text{sub}}$  states ② and ⑥ in Fig. 1. The surface of demarcation between externally and internally occurring shocks corresponds to state ④ in the exit nozzle plane where  $p_{\text{sup}}$  may be calculated using the normal shock relation given by:

$$P = 2\varepsilon\gamma \left[ \left( \frac{2}{\gamma+1} \right) \left( 1 + \frac{\gamma-1}{4\gamma} P \right) \right]^{\frac{\gamma+1}{\gamma-1}} \quad (2)$$

where  $P$  is the pressure change across a shock,  $\bar{p}^+ / \bar{p}^-$ , with  $\bar{p}^+$  being the larger pressure after the shock and  $\bar{p}^-$ , the smaller pre-shock pressure. This relation may be tied to the chamber pressure via the supersonic branch of the isentropic pressure expansion used to calculate the previous curves. The equations themselves are transcendental to the extent of requiring numerical solutions. However, using asymptotic methods,<sup>6</sup> a set of analytical approximations may be developed that are accurate for expansion ratios common to most propulsive applications. The solutions may be readily returned from a recursive form, and as such can be calculated to an arbitrary level of precision. In practice, most propulsive applications only require two terms for a solution with acceptable engineering accuracy.

### A. Inverse Isentropic Formulation

To demonstrate the flexibility of the asymptotic methods employed here, we solve both the isentropic and shock equations with the chamber pressure in the numerator. This approach is preferred over solving the ratio with the chamber pressure in the denominator and then inverting the solution. First, after some manipulation, Eq. (1) can be rewritten as

$$p^\alpha - p^\beta = \varepsilon\xi \quad (3)$$

Here  $\alpha \equiv -2/\gamma$ ,  $\beta \equiv -1-1/\gamma$ , and

$$\xi \equiv \frac{\gamma-1}{2} \left( \frac{2}{\gamma+1} \right)^{\frac{\gamma+1}{\gamma-1}} = \frac{\gamma-1}{\gamma+1} \left( \frac{1}{\gamma+1} \right)^{\frac{2}{\gamma-1}} \quad (4)$$

Determining the subsonic root of Eq. (3) requires a regular perturbation expansion which, to arbitrary precision, can be expressed as

$$p = p_0 + \varepsilon p_1 + \varepsilon^2 p_2 + \dots + \varepsilon^{n-1} p_{n-1} + O(\varepsilon^n) \quad (5)$$

Equation (5) may be substituted into Eq. (3) and then expanded. For the reader's convenience the expanded equation is presented below at  $O(\varepsilon^2)$ :

$$p_0^\alpha - p_0^\beta + \varepsilon(\alpha p_1 p_0^{\alpha-1} - \beta p_1 p_0^{\beta-1} - \xi) + O(\varepsilon^2) = 0 \quad (6)$$

Because these quantities must vanish identically for all values of  $\varepsilon$ , we can segregate Eq. (6) into  $n$  separate equations and then solve them in series for the individual values of  $p$  at each order. This produces

$$p = 1 + \varepsilon \left( \frac{\xi}{\alpha - \beta} \right) + \varepsilon^2 \left[ \frac{\xi^2 (\alpha + \beta - 1)}{2(\alpha - \beta)^2} \right] + \varepsilon^3 \left[ \frac{\xi^3 (2\alpha + \beta - 1)(\alpha + 2\beta - 1)}{6(\alpha - \beta)^3} \right] + \varepsilon^4 \left[ \frac{\xi^4 (2\alpha + 2\beta - 1)(\alpha + 3\beta - 1)(3\alpha + \beta - 1)}{24(\alpha - \beta)^4} \right] + O(\varepsilon^5) \quad (7)$$

Owing to the judicious choice of  $\alpha$  and  $\beta$ , Eq. (7) duplicates that which appears in our previous study. However, the actual rate of convergence is different here. As expected, the ratio with the chamber pressure in the denominator converges more quickly than in the inverse case. Practically, the disparities in convergence are relatively small and become indiscernible when carried out to  $O(\varepsilon^5)$ . At the outset, excellent agreement may be expected even with the slower converging approach in which the larger chamber pressure appears in the numerator.

The supersonic root can be handled in a similar fashion. Equation (3) provides the relation for the new, inverted pressure ratio. Keeping with the generalized constants, we find that, after substitution and binomial expansion, Eq. (3) becomes

$$p_0^\alpha \left[ 1 + \alpha(p_1 / p_0) + O(p_1 / p_0)^2 \right] - p_0^\beta \left[ 1 + \beta(p_1 / p_0) + O(p_1 / p_0)^2 \right] - \varepsilon \xi = 0 \quad (8)$$

When solved for  $p_1$ , Eq. (8) returns

$$p_1 = \frac{p_0 \left[ p_0^\alpha - p_0^\beta - \varepsilon \xi \right]}{\beta p_0^\beta - (2/\gamma) p_0^\alpha} \quad (9)$$

which is similar to the form derived in the previous study, albeit with generalized constants. Additional terms can be calculated via the recursive relation

$$p_m = \frac{\left( \sum_{j=0}^{m-1} p_j \right)^\alpha - \left( \sum_{j=0}^{m-1} p_j \right)^\beta - \varepsilon \xi}{\beta \left( \sum_{j=0}^{m-1} p_j \right)^{\beta-1} - \alpha \left( \sum_{j=0}^{m-1} p_j \right)^{\alpha-1}} \quad (10)$$

The total solution for pressure consists of the summation of the individual orders, starting with the leading-order approximation, namely

$$p_{\text{opt}}(\varepsilon, \gamma, n) = p_0 + \sum_{m=1}^n p_m \quad (11)$$

The solutions for both branches are compared in Table 1. Much like the subsonic solution, the inverse solution shows a somewhat slower convergence rate as increasing numbers of terms are retained. In fact, the difference becomes quite small after three terms. The reader is cautioned, however, that care must be taken when using this formulation, rather than the solution derived in Part 1. As  $\varepsilon$  increases and  $\gamma$  decreases it is possible to violate the principle of least singular behavior and thus render the solution invalid. A coupling of the embedded dependence of  $\varepsilon$  and  $\gamma$  and pressure ratios greater than 1 in the present supersonic solution can lead to unphysical behavior. Such an issue does not affect the subsonic solution, as the explicit gauge functions prevent it from occurring.

**Table 1. Comparison of Part 1/Part 2 solutions using  $\gamma=1.6$**

		Subsonic, $p_{\text{sub}}$		Supersonic, $p_{\text{opt}}$	
$\varepsilon \backslash n$		1	3	1	3
0.05		1.0130	1.0132	58.645	58.764
		1.0128	1.0132	55.840	58.764
0.1		1.0263	1.0270	31.739	31.798
		1.0256	1.0270	29.007	31.796
0.3		1.0834	1.0910	11.355	11.281
		1.0770	1.0906	8.5034	11.250
0.5		1.1472	1.1732	6.7619	6.5728
		1.1283	1.1702	3.6792	6.4902

### B. Inverse Shock Formulation

The shock pressure relation is already inverted in a manner of speaking. Because of the changes in variable used in the previous study, namely  $P = p(\gamma + 1) + \gamma - 1$  and  $X = 1/P$ , the problem is already inverted to the faster converging solution, which in this case is also the  $\bar{p}^- / \bar{p}^+$  type solution. For the sake of completeness, the slower converging solution is presented here. The corresponding route follows a similar procedure but does not invoke the  $X = 1/P$  variable change. The resulting governing equation becomes

$$P = 2\varepsilon\gamma \left[ \frac{2}{\gamma+1} \left( 1 + \frac{\gamma-1}{4\gamma} P \right) \right]^{\frac{\gamma+1}{\gamma-1}} \quad (12)$$

The leading-order term in Eq.(12) may be found by balancing the dominant terms of the equations; in this case, we extract

$$2\varepsilon\gamma \frac{\gamma-1}{\gamma+1} P_0^{\frac{\gamma-1}{\gamma+1}} = \frac{\gamma-1}{2\gamma(\gamma+1)} P_0 \quad (13)$$

which, in turn, yields

$$P_0 = 2\gamma\varepsilon^{\frac{1-\gamma}{2}} \left( \frac{\gamma+1}{\gamma-1} \right)^{\frac{\gamma+1}{2}} \quad (14)$$

The remaining terms can be calculated using successive approximations. For the first-order correction, we have

$$(P_0 + P_1)^{\frac{\gamma-1}{\gamma+1}} = (2\varepsilon\gamma)^{\frac{\gamma-1}{\gamma+1}} \left( \frac{2}{\gamma+1} \right) \left[ 1 + \frac{\gamma-1}{4\gamma} (P_0 + P_1) \right] \quad (15)$$

The solution for  $P_1$  can be found using the same binomial expansion technique,

$$P_1 = \frac{(2\varepsilon\gamma)^{\frac{\gamma-1}{\gamma+1}} \left( \frac{2}{\gamma+1} \right) + (2\varepsilon\gamma)^{\frac{\gamma-1}{\gamma+1}} \left[ \frac{\gamma-1}{2\gamma(\gamma+1)} \right] P_0 - P_0^{\frac{\gamma-1}{\gamma+1}}}{\frac{\gamma-1}{\gamma+1} P_0^{-\frac{2}{\gamma+1}} - (2\varepsilon\gamma)^{\frac{\gamma-1}{\gamma+1}} \left[ \frac{\gamma-1}{2\gamma(\gamma+1)} \right]} \quad (16)$$

or

$$P_1 = \left[ c_1 \left( \frac{2}{\gamma+1} \right) + c_1 c_2 P_0 - P_0^{\frac{\gamma-1}{\gamma+1}} \right] \left( \frac{\gamma-1}{\gamma+1} P_0^{-\frac{2}{\gamma+1}} - c_1 c_2 \right)^{-1} \quad (17)$$

where

$$c_1 = (2\varepsilon\gamma)^{\frac{\gamma-1}{\gamma+1}} \quad c_2 = \frac{\gamma-1}{2\gamma(\gamma+1)} \quad (18)$$

Higher-order terms can be precipitated from the recursive expression,

$$P_n = \left[ c_1 \left( \frac{2}{\gamma+1} \right) + c_1 c_2 \sum_{i=1}^{n-1} P_i - \left( \sum_{i=1}^{n-1} P_i \right)^{\frac{\gamma-1}{\gamma+1}} \right] \left[ \frac{\gamma-1}{\gamma+1} \left( \sum_{i=1}^{n-1} P_i \right)^{-\frac{2}{\gamma+1}} - c_1 c_2 \right]^{-1} \quad (19)$$

With the addition of Eq. (19), a comparison between the inverted and noninverted values can be conducted. The inverted values in this case converge more quickly as they consist of the solution that employs the smaller ratio of the two. Again the larger ratio is found to converge more slowly, although the error between them becomes negligible after a handful of terms.

### III. Results and Discussion

With these one-dimensional boundary values in hand, it is possible to evaluate existing performance data with the goal of examining the operating pressure ratios during blowdown. It is also possible to determine the range and duration of the pressure variation through which the profile remains susceptible of generating sideloads. In this vein, the relationships in Table 2 can be plotted versus the expansion ratio of the nozzle to provide a map of the operating boundaries as the pressure ratio across the nozzle varies. Figure 3 displays the boundary curves that make up the nozzle map. The regions are labeled consistently with Figs. 1 and 2. Therein, analytical expressions with a limited number of terms are compared to the numerical solution to provide a comprehensive map for the nozzle transition points. It is clear that, for the high expansion ratios common to most propulsion configurations, a few terms of the analytical approximation provide adequate accuracy relative to a numerical solution.

#### A. Nozzle Operational Modes and Chamber Pressure

As mentioned above, Fig. 3 enables us to identify different nozzle operating modes over a range of back pressure values. In area ① the nozzle is under-expanded and expansion fans occur in the exit plane as the relatively higher pressure fluid seeks to match ambient conditions. Area ③ introduces external oblique shocks and one-dimensional theory no longer provides an accurate assessment of the flowfield. In area ⑤, the shock activities become internal and the flow undergoes a normal standing shock at some location within the nozzle. Finally in area ⑦, the flow throughout the nozzle turns subsonic. The unbounded nature of the nozzle shock and optimal expansion curves for small values of  $\varepsilon$  increase the size of computations in the propulsive range of expansion ratios.

In complementing the data on this graph, we reproduce in Fig. 4 the same nozzle map using the pressure convention adopted in Part 1 wherein all ratios are referenced to the chamber pressure. As a result, the unbounded behavior is eliminated and both pressure and  $\varepsilon$  are scaled on a [0,1] interval. It is interesting to note that the relative size of the operating modes does not remain constant. On the one hand, the normal shock zone ⑤ displays inverse behavior with the normal shock increasing as  $\varepsilon$  decreases. On the other hand, the oblique shock region ③ maintains a relatively constant size for most expansion ratios, closely resembling a semi-oval with the only large excursions appearing for substantially small or large expansion ratios. For most propulsive applications, the expansion ratios would produce values of  $\varepsilon$  that are well below 0.1. During the transient stages of operation, the internal shock region has a much larger pressure ratio range than the external one. This may explain the increased internal shock activities and separation patterns that may occur inside the nozzle during blowdown, events that contribute to the propensity of undesirable sideloads.

**Table 2. Summary of one-dimensional relations for nozzle flow characterization**

Boundary name	Asymptotic approximation
Choking Boundary ⑥	$p_{\text{sub}} = \frac{\bar{p}_{\text{sub}}}{\bar{p}_e} = - \sum_{m=0}^n \frac{\prod_{j=1}^{m-1} [(m-j)\alpha + j\beta - 1]}{(-1)^{(2m)!} m! (\beta - \alpha)^m} (\varepsilon \xi)^m + O(\varepsilon^{n+1})$
Optimal Design ②	$p_{\text{opt}} = \frac{\bar{p}_{\text{opt}}}{\bar{p}_e} = \varepsilon \xi + \sum_{m=1}^n p_m \text{ where}$ $p_m = \frac{\left( \sum_{j=0}^{m-1} p_j \right)^{2/\gamma} - \left( \sum_{j=0}^{m-1} p_j \right)^{(\gamma+1)/\gamma} - \varepsilon \xi}{\frac{\gamma+1}{\gamma} \left( \sum_{j=0}^{m-1} p_j \right)^{1/\gamma} - \frac{2}{\gamma} \left( \sum_{j=0}^{m-1} p_j \right)^{2/\gamma-1}}$
Nozzle Shock ④	$p_{\text{sup}} = \frac{\bar{p}_{\text{sup}}}{\bar{p}_e} = \frac{1}{(\gamma+1)X} - m \text{ where}$ $X = X_0 + \sum_{k=1}^n X_k; X_k = \frac{(\varepsilon \gamma x_k)^m (ax_k + b) - x_k}{1 - \varepsilon^m x_k^m [a(m+1) + bm x_k^{-1}]}; x_k \equiv \sum_{j=0}^{k-1} X_j$

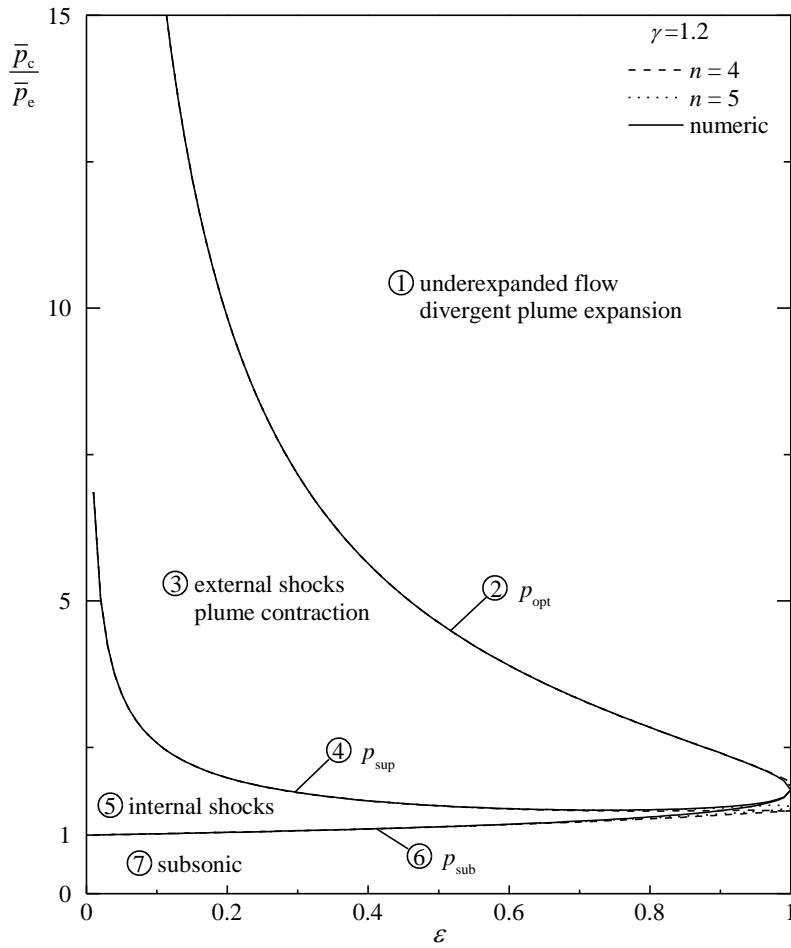


**Figure 3. Pressure map versus  $\varepsilon$  during chamber blowdown. The vertical axis represents the chamber-to-exit pressure ratio.**

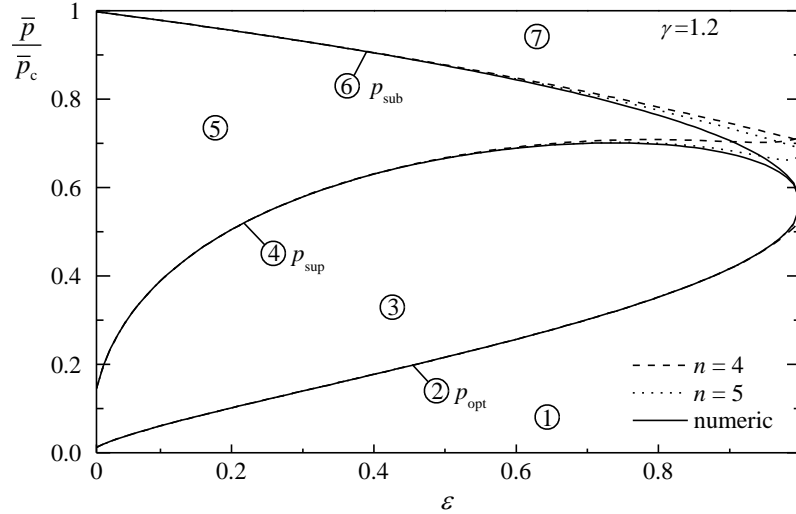


Figure 4. Inverted pressure map versus  $\varepsilon$  using the chamber pressure as a benchmark.

### B. Other Considerations

The present study is not meant to be a comprehensive investigation into blowdown, but rather a first step towards a generalized analytical framework for its modeling and prediction. While the one-dimensional equations treated here provide general breakpoints for nozzle behavior, the limitations of the analysis prevent it from predicting blowdown sideloads. For example, experimental investigations have found that separation inside a nozzle and its associated sideloads are influenced by the local nozzle contour.<sup>7</sup> The present study cannot account for such variation without further investigation. Moreover, the asymmetric nature of the separation process causing sideloads requires at least a modified two-dimensional approach in order to make any sort of prediction possible. Finally, in addition to the steady-state sideloads, oscillatory loads can be experienced during blowdown,<sup>8</sup> and these would require a time-dependence that the present model lacks. The goal of future development is to focus on the specific regime where internal shocks and separations can occur and to use asymptotic methods to develop multi-dimensional formulations that can better accommodate the physical mechanisms that induce the additional loads observed during blowdown.

### C. Motor Blowdown Data and Slag Accumulation

In a recent investigation, flight telemetry acquired from a sounding rocket motor has showed a significant increase in roll torque as propellant burnback reached its terminal phase. The motor in question was approximately 17-inches in diameter and 210-inches long including the nozzle. The propellant was aluminized and hence produced a substantial amount of slag during motor burn. The motor itself formed the upper stage of a spin-stabilized sounding rocket. At its nominal operating altitude, aerodynamic drag acting on the stabilizing fins became so small that it took less vortical force on the nozzle inner wall to increase the vehicle spin rate. Furthermore, the grain design had two opposed slots as shown in Fig. 5 below. Based on the burnback cross-sections, it can be seen that near motor blowdown, two opposed pools of slag materialized. These were retained behind the final increment of propellant and appeared to be trapped on the case wall due to the centrifugal force exerted by the spinning motor.

The spin rate of the motor and its corresponding pressure trace during tail off are displayed in Fig. 6 as a function of flight time. As it can be seen, the declining motor pressure started around  $t = 31$  seconds and

triggered a *linear doubling* of roll frequency as the chamber gases blew down. Radar and accelerometer data indicated that a massive expulsion of slag was also initiated simultaneously at 31 seconds due to its sudden volumetric expansion from dissolved chamber gases. It was speculated that the slag-laden gas might be swirling at this point to the extent of inducing roll torques that were sufficiently large to cause the vehicle to spin in response to wall friction with the vortex.

In fact, the sudden accumulation of slag after tail off could be exacerbated by corner circulation and the drop in pressure and temperature in the chamber. These factors can promote solidification of the gaseous fraction of aluminum oxide remaining in the chamber.

A theoretical explanation of the observed behavior is this. During normal operation, the high pressure in the motor ensures choking conditions and supersonic expansion in the axial direction. Transonic expansions through the nozzle are dominated by axial motion, thus rendering the effects of the normal

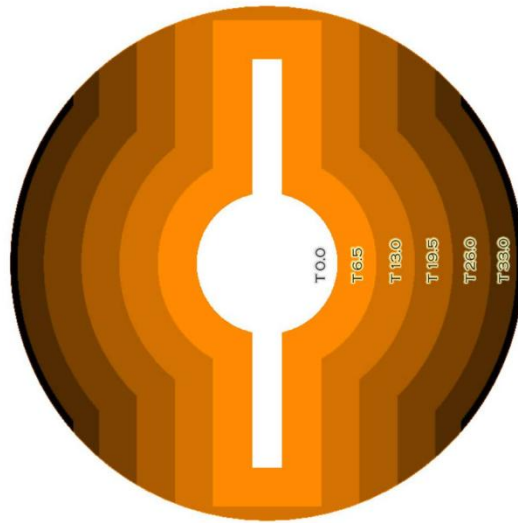


Figure 5. Grain burnback cross-section versus time (sec) for a sounding rocket upper stage.

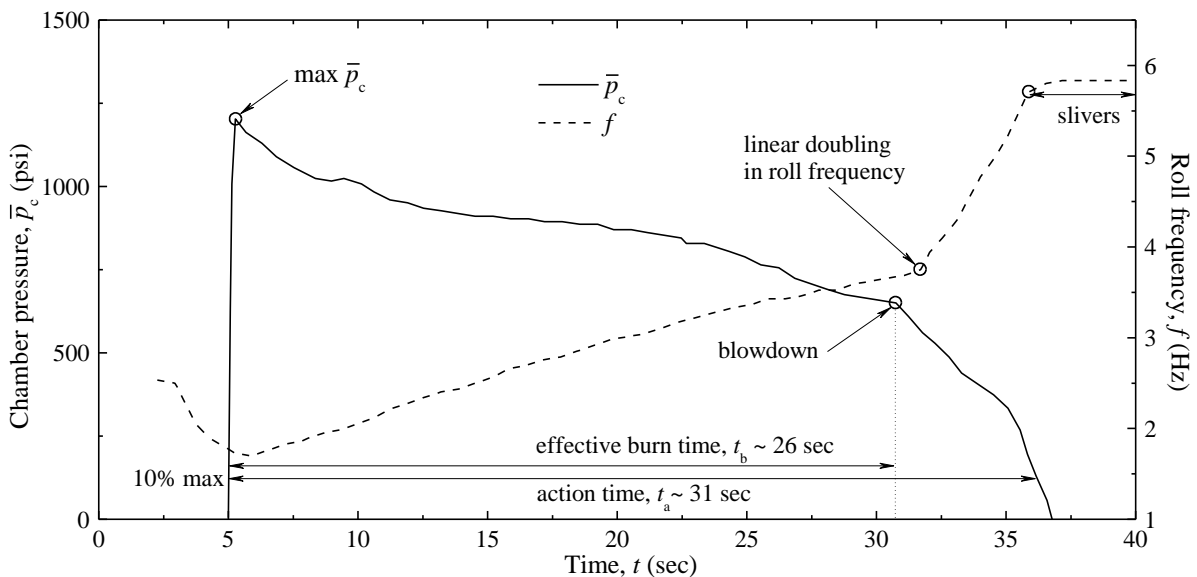


Figure 6. Grain burnback pressure trace and roll frequency versus time for a sounding rocket upper stage.

(cross-streamwise) and tangential (spin) components negligible in comparison. After blowdown, this scenario changes in that, as the pressure drops, so will the axial velocity. Suddenly, one may notice an increase in roll, pitch, and yaw. This behavior can be attributed to the resurgence of the tangential and normal forces as non-negligible contributors. In addition, a bathtub vortex is typically formed while emptying, thus causing the spin velocity to become even more appreciable. From this perspective, the spiraling motion of the slag-laden mixture through the nozzle may be partly responsible for the increase in roll. When the normal and tangential forces are no longer negligible (i.e., when they become of the same relative order as the depreciating axial force), sudden redirections in pitch and yaw may be felt throughout the motor, in addition to a doubling in roll with the passage of time. As shown in Fig. 6, the sustained doubling in roll frequency occurs shortly after the initiation of pressure blowdown. The linear increase in  $f$  continues until reaching the time that marks the beginning of the sliver burn period. This phase is accompanied by a substantial diminishment in thrust along with a horizontal flattening in the roll frequency.

Regarding the pressure trace in Fig. 6, it should be noted that three threshold values may be useful to point out. The first corresponds to the chamber pressure  $\bar{p}_{\text{sup}}$  for which a shock will occur in the nozzle exit plane. Any pressure below that value will induce shocks within the nozzle. These shocks are susceptible to spiral around and cause random lateral moments that can, in turn, induce fluctuations in pitch, yaw, and roll. The second threshold pressure will be the minimum chamber pressure  $\bar{p}_{\text{sub}}$  that will still induce choked conditions at the throat. Below that reference value, the flow becomes subsonic throughout. In the process, the supersonic axial velocity magnification in the streamwise direction will cease to occur. The swirling angular momentum becomes of the same order at that of the axial component, and this condition can develop when the chamber pressure drops below 1.894 times the outer pressure. In the present investigation, the determination of  $\bar{p}_{\text{sup}}$  and  $\bar{p}_{\text{sub}}$  requires instantaneous values for the external pressure and nozzle area ratio.

#### IV. Concluding Remarks

In summary, two threshold pressure ratios are important to note. The first,  $\bar{p}_{\text{sup}}$ , corresponds to the chamber pressure for which a shock will occur right in the nozzle exit plane. Any chamber pressure below that point will induce shocks inside the nozzle. These shocks can spiral around and cause random lateral moments, thus inducing fluctuations in pitch, yaw, and roll. The next threshold pressure will be the minimum chamber pressure,  $\bar{p}_{\text{sub}}$ , that will still induce choked conditions at the throat. Below that value, the flow will turn subsonic everywhere. At that moment the supersonic axial velocity increase in the streamwise direction will no longer occur. The swirling angular momentum becomes of the same order at that of the axial. In practice, this situation unfolds when the chamber pressure falls under 1.894 times the outer pressure.

Today, most nozzle transient predictions are conducted using empirical methods derived from correlating engine tests, as in the skewed plane method,<sup>9</sup> or through numerical simulations.<sup>10,11</sup> An improved analytical framework can help to guide these experimental and numerical investigations, as well as provide insight into the physical processes that stand behind these transient phenomena. Future research efforts would include incorporation of two-dimensional effects as well as oscillatory models to account for both the steady and unsteady forces observed during the blowdown process. It will be helpful to investigate these effects further as it seems that they have been judiciously avoided in the past.

#### Acknowledgments

This work was completed with the support of the National Science Foundation through Grant No. CMMI-0928762.

## References

- <sup>1</sup>Anon., “4400-Hz Vibration Investigation, Final Report,” Rocketdyne, Canoga Park, CA, June 1971.
- <sup>2</sup>Winterfeldt, L., Laumert, B., Tano, R., Geneau, J. F., Blasi, R., and Hagemann, G., “Redesign of the Vulcain 2 Nozzle Extension,” AIAA Paper 2005-4536, July 2005.
- <sup>3</sup>Watanabe, Y., Sakazume, N., and Tsuboi, M., “LE-7A Engine Separation Phenomenon Differences of the Two Nozzle Configurations,” AIAA Paper 2003-4763, July 2003.
- <sup>4</sup>Watanabe, Y., Sakazume, N., and Tsuboi, M., “LE-7A Engine Nozzle Problems During the Transient Operations,” AIAA Paper 2002-3841, July 2002.
- <sup>5</sup>Holland, W., “SSME/Side Loads Analysis for Flight Configuration,” NASA Marshall Space Flight Center, Technical Rept. TM-X-6484, Huntsville, AL, September 1974.
- <sup>6</sup>Maicke, B. A., and Majdalani, J., “Pressure Variations in Rocket Nozzles. Part 1: Direct Asymptotic Predictions,” AIAA Paper 2010-7072, July 2010.
- <sup>7</sup>Hagemann, G., Frey, M., and Koschel, W., “Appearance of Restricted Shock Separation in Rocket Nozzles,” *Journal of Propulsion and Power*, Vol. 18, No. 3, 2002, pp. 577-584. [doi: 10.2514/2.5971](https://doi.org/10.2514/2.5971)
- <sup>8</sup>Deck, S., and Guillen, P., “Numerical Simulation of Side Loads in an Ideal Truncated Nozzle,” *Journal of Propulsion and Power*, Vol. 18, No. 2, 2002, pp. 261-269. [doi: 10.2514/2.5965](https://doi.org/10.2514/2.5965)
- <sup>9</sup>Shi, J., “Rocket Engine Nozzle Side Load Transient Analysis Methodology: A Practical Approach,” AIAA Paper 2005-1860, April 2005.
- <sup>10</sup>Wang, T.-S., “Transient Three-Dimensional Startup Side Load Analysis of a Regeneratively Cooled Nozzle,” *Shock Waves*, Vol. 19, 2009, pp. 251-264. [doi: 10.1007/s00193-009-0201-2](https://doi.org/10.1007/s00193-009-0201-2)
- <sup>11</sup>Shimizu, T., Miyajima, H., and Kodera, M., “Numerical Study of Restricted Shock Separation in a Compressed Truncated Perfect Nozzle,” *AIAA Journal*, Vol. 44, No. 3, 2006, pp. 576-584. [doi: 10.2514/1.14288](https://doi.org/10.2514/1.14288)